A fresh perspective on ENSO nonlinearity: the ENSO pattern continuum metric

Sulian Thual, Boris Dewitte

npj | climate and atmospheric science

Article

Published in partnership with CECCR at King Abdulaziz University

https://doi.org/10.1038/s41612-025-01233-3

A fresh perspective on ENSO nonlinearity: the ENSO pattern continuum metric

Sulian Thual[1,2] ✉ & Boris Dewitte[3,4,5]

The El Niño-Southern Oscillation (ENSO) is characterized by a zonal (longitudinal) displacement of the background Walker circulation across the equatorial Pacific, or spatial shifting. The warm pool edge position (WPEP) commonly measures the intensity of this shifting. Hereby organizing sea surface temperature (SST) maps according to WPEP quantiles, we construct a synthetic, continuous sequence of patterns—termed the pattern continuum—that captures the SST evolution along the movement, namely the gradual transition from broad Central Pacific La Niña cooling to Central then Eastern Pacific El Niño warming. This pattern continuum can also be approximated by a "shifted-mean" framework, wherein a fixed spatial structure shifts zonally. The present diagnosis provides insight into key dynamical features of the ENSO, such as its spatial diversity, asymmetry, and nonlinearity, including the quadratic relationship between SST principal components. It may also be useful for practical model evaluation and intercomparison.

The ENSO, which consists of the alternation of El Niño and La Niña events in the equatorial Pacific, is the dominant interannual mode of climate variability on Earth, and it has major global impacts on societies and ecosystems[1,2]. Long-range prediction of ENSO remains a major challenge[3], largely due to its multifaceted nature—often referred to as ENSO complexity[4]—which encompasses its diversity, non-linearity, asymmetry, and interactions with other ocean basins beyond the tropical Pacific. Although each ENSO event is unique, sea surface temperature (SST) tends to exhibit Central Pacific (CP) or Eastern Pacific (EP) warming during El Niño and more basin-wide cooling during La Niña (diversity)[5–7]. In addition, SST warming can sometimes be very intense during El Niño (nonlinearity) while the reverse is not true for La Niña (asymmetry)[8]. These features are fundamental for ENSO prediction, teleconnections, and impacts, as well as for grasping its dynamics, yet remain partly elusive.

During El Niño or La Niña, there is also a marked zonal (i.e., longitudinal) displacement of the ocean and atmosphere circulation in the equatorial Pacific (i.e., Walker circulation[9]), which we denote here as spatial shifting[10]. This process can be measured, for example, by the warm pool edge position (WPEP), typically taken as the 28.5 °C isotherm[11] (or 29 °C isotherm as in the present paper, see "Methods" section), but it also displaces broad ocean and atmosphere structures (e.g. of SST, winds, currents, precipitation, thermocline depth, and so on[12,13]).

Several theoretical models describe the relationship between spatial shifting (or at least WPEP changes) and ENSO dynamics[13,14], including a recent theoretical model from the authors[10] denoted hereafter as TD23 (for "Thual and Dewitte 2023"). In particular, TD23 proposes that when the Walker circulation shifts along with WPEP, its geometrical structure relative to the WPEP is approximately conserved on field totals along the equator—that is, that spatial shifting is approximately conservative. An earlier form of the mechanism can also be found in ref. 15. While the mechanism is rather elementary, it has surprisingly important dynamical implications. A flow in which a conserved spatial structure shifts over time is rather simple, yet its anomalies (computed by removing the temporal mean) can be dynamically rich with potentially spatio-temporal nonlinearity, asymmetry, pattern diversity, and so on[10,15]. For instance, by combining the process with conventional recharge-discharge dynamics[16,17], the TD23 model captures a baseline level of ENSO diversity and asymmetry that closely mirrors many observed features. However, the model's idealized geometry necessarily limits its realism.

While spatial shifting is a central feature of ENSO variability, there are few available methods to quantify it precisely in observations or climate data in general. The WPEP, while useful at measuring the intensity of the spatial shifting movement itself[11,18], does not quantify the spatio-temporal evolution of the broad ocean and atmosphere structures involved in the movement. We may want to quantify, for example, how these structures evolve relative to the WPEP[19,20], and to what extent they are geometrically conserved (i.e., to what extent the TD23 approximation holds[10]). There is also a need to quantify the relationship between spatial shifting and the features of ENSO complexity mentioned above. It has been proposed, for example, that El Niño events organize into a continuum of SST warmings

[1]Mercator-Ocean International, Toulouse, France. [2]School of Computing, Clemson University, 100 McAdams Hall SC Clemson, USA. [3]CECI, Université de Toulouse, CERFACS, CNRS, Toulouse, France. [4]Centro de Estudios Avanzados en Zonas Aridas (CEAZA), La Serena, Chile. [5]Departamento de Biología Marina, Facultad de Ciencias del Mar, Universidad Católica del Norte, Coquimbo, Chile. ✉e-mail: sulian.thual@gmail.com

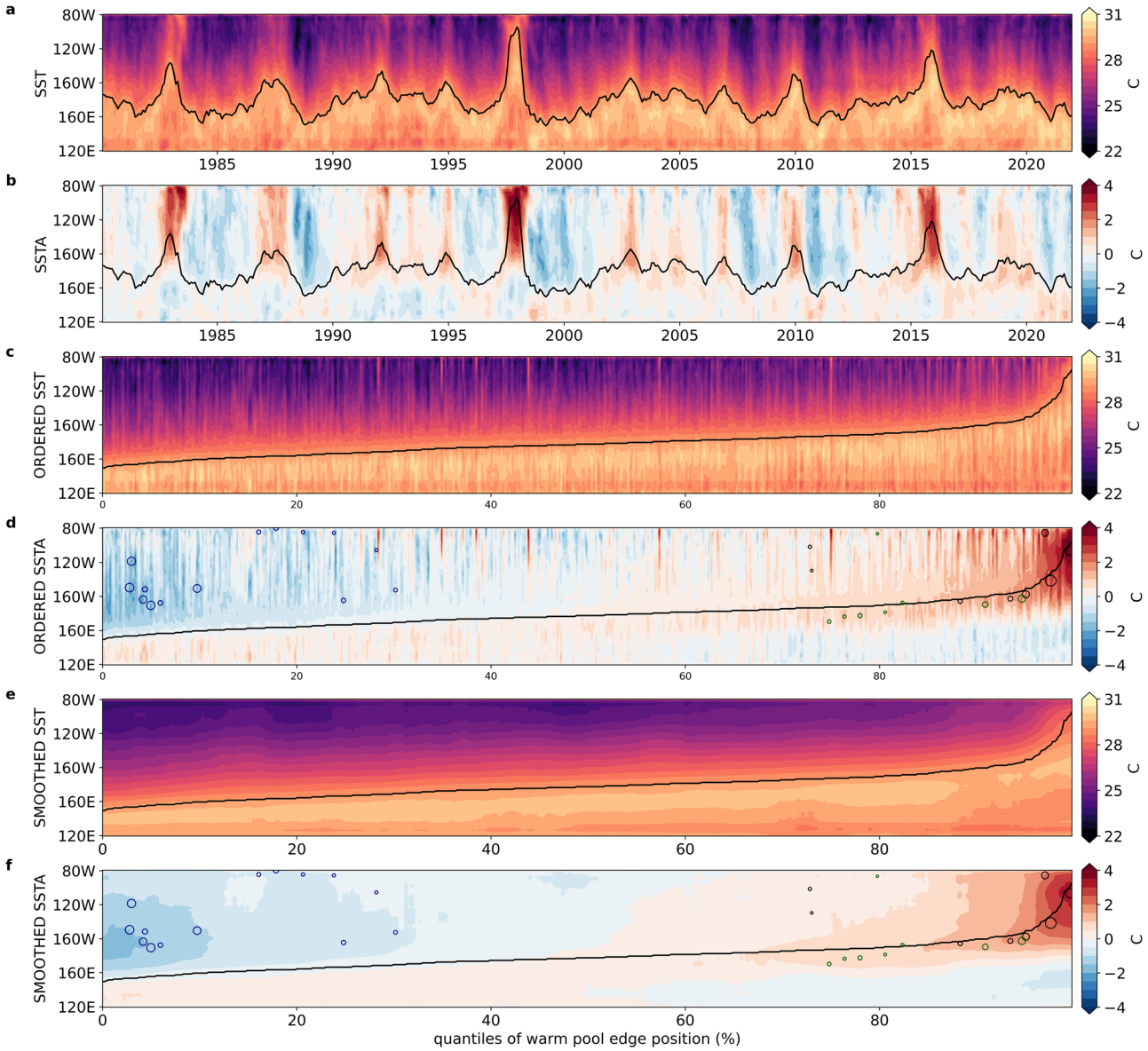

Fig. 1 | Derivation of the SST pattern continuum. a Hovmoller of SST in the Tropical Pacific (average 5° N–5° S), with seasonal variations removed and as a function of time (in years) and longitude. The black line indicates WPEP, roughly estimated from the 29 °C isotherm (see "Methods" section). **b** Same as a, but for SST anomalies (SSTA). **c** SST from (**a**) ordered by quantiles of WPEP (in %), thus with monotonous increase of WPEP (black line). **d** SSTA from (**b**) ordered by quantiles of WPEP (in %). Circles indicate individual ENSO events at their peak (Dec-Jan-Feb averages) in terms of longitude of max warming/cooling (circle position), overall intensity (circle size proportional to Niño 3.4 SSTA), and type (circle color: blue for La Niña, green for CP El Niño, and black for EP El Niño). **e**, **f** Same as (**c**, **d**), but quantile smoothed (i.e., smoothed horizontally) with a running-mean of 25 samples (circles from d are repeated). The quantile ordering and smoothing reveals spatial shifting on SST that approximately conserves structures, and gradual transitions between ENSO patterns on SSTA.

that peak anywhere between the central to EP, rather than into completely distinct CP and EP types[21]. The longitude of SST warming is, in fact, tied to spatial shifting intensity, that is, to WPEP as well as to the longitude for deep convection within the Walker circulation[10,22].

For these reasons, we propose here a series of new diagnoses aimed at evaluating ENSO spatial shifting in climate data. For the sake of brevity and simplicity, our analysis in this paper is restricted to SST observations in the equatorial band, with seasonal variations omitted. The paper is organized as follows. In the results section, we first diagnose changes in SST patterns with spatial shifting through a quantile-plot denoted as "pattern continuum". We then derive a simplified nonlinear SST flow, denoted as shifted-mean flow, that approximates the observed SST flow. In light of this simplified framework, we also interpret a commonly used metric for diagnosing ENSO nonlinearity, namely the quadratic relationship between the leading principal components of SST. In the discussion section, we summarize the main takeaways and also briefly extend our analysis to a long-term simulation from a general circulation model. The methods section provides further material.

Results

Pattern continuum

In this section, we propose a synthetic representation of SST pattern diversity, called "pattern continuum", that is based on WPEP quantiles. We consider monthly SST observations from the GODAS reanalysis[23], with seasonal variations removed, for which we compute SST totals and SST anomalies (SSTA) averaged in the equatorial band (5° N–5° S, see "Methods" section). Looking at SST totals (Fig. 1a), the equatorial Pacific can be roughly delineated into a western "warm pool" region with SSTs saturating around 30 °C, and an eastern "cold tongue" region with gradually cooling SSTs. These regions are delineated by the WPEP that here roughly corresponds to

the 29 °C isotherm[11,22] (see "Methods" section). As the WPEP varies during El Niño and La Niña events, the regions move zonally (as well as expand or contract), which is the spatial shifting process (see TD23). On the other hand, SST anomalies (Fig. 1b) show episodic patterns of warming/cooling, with considerable diversity but generally organized into broad La Niña cooling, central El Niño warming, as well as (sometimes extreme) EP El Niño warming.

Here, we want to address how the pattern diversity of SST anomalies relates to the spatial shifting of SST totals. To address this, we order the monthly SST and SSTA samples (Fig. 1a, b) by increasing quantile of WPEP (Fig. 1c, d), then sample-smooth using a running mean of 25 samples (≈ 5% of total sample size) to denoise the figures (Fig. 1e, f). Other sample-smoothing methods may be equivalently considered. WPEP (black lines in Fig. 1) increases monotonically with quantiles by definition, ranging roughly from 160° E to 90° W. The present representations, which we denote as pattern continuums, allow visualizing pattern modifications with respect to an axis, here spatial shifting intensity or WPEP. When smoothed, they become data composites in which WPEP entirely determines the SST profile. In that case, they measure the canonical (or average) evolution of SST with respect to spatial shifting intensity[7].

The present pattern continuums reveal a fundamental organization of SST versus SSTA variations, in which elementary SST variations appear to be intrinsically more complex on SSTA. The SST smoothed pattern continuum in fact simply shows the gradual shifting of the warm pool and cold tongue regions with WPEP (Fig. 1e). The SSTA smoothed pattern continuum in contrast grasps major elements of ENSO complexity (Fig. 1f). For instance, it captures all major patterns of ENSO diversity, with rather gradual and coherent transitions between them[5,6]. We distinguish first the La Niña range (0–30th quantiles) where broad cooling extends from the WPEP to the EP border and is centered around 160° W. Second is the range of neutral conditions (30–70th quantiles), with weak anomalies but a reversal of EP cooling to warming and western Pacific warming to cooling. Third is the CP El Niño range (70–90th quantiles) with a moderate but gradually intensifying warming that remains centered on the WPEP (and thus gradually shifts eastward). Fourth and last is the EP El Niño range (90th–100th quantiles), with strong warming also centered on the WPEP. The gradual transitions here support the notion that ENSO diversity organizes into a continuum of events rather than into completely separate event types[5,6,21] (EP vs CP, and strong vs moderate). El Niño SSTA warming, for example, may here be found gradually stronger and more eastward within the continuum[21]. The SSTA smoothed pattern continuum is also fundamentally asymmetric between low and high quantiles, consistent with ENSO asymmetry in nature[8,24]. For instance, La Niña cooling extends more westward than El Niño warming, and there is no clear pattern associated with EP La Niña cooling[25,26]. Rare extreme EP El Niño events are also much more intense. As another example of asymmetry, WPEP is skewed towards rare but extreme eastward displacements above the 90th quantile (technically, the quantile plot deviates from a probit function implying a non-Gaussian distribution).

Within the realm of existing metrics for ENSO characterization[21], we can situate pattern continuums as compact (i.e., univariate[22] instead of multivariate[6,24,26]), continuum-based (i.e., smooth instead of thresholded or clustered[6]), spatial (instead of region-averaged), and SST-based (at least in the present paper), which has its own advantages. The smoothed pattern continuums (Fig. 1e, f), however, do not capture the full range of SST variations in nature (Fig. 1c, d), and as such should be interpreted with some caution. Comparing Fig. 1d, f, there are discrepancies mostly in the far EP. They may correspond to specific ENSO events for which WPEP is unrepresentative of the SSTA warming/cooling pattern[6], or just non-ENSO variability in the broad sense (e.g., higher-frequency or localized variability, etc.[27,28]). The main discrepancies are in fact found mid-1983 and mid-1998, in the aftermath of two extreme El Niño events (see "Methods" section). During these periods, warm SSTs lingered unusually long in the far EP while the WPEP shifted back westward: this was likely due to strong meridional wind shifting preventing seasonal surface cooling, a nonlinear mechanism separate from the present zonal spatial shifting[29–32]. Nevertheless, the correspondence with individual samples is reasonable overall. As another example of this, unsmoothed CP/EP El Niño events tend to peak just west of the WPEP, while La Niñas peak in the CP, which aligns with the pattern continuum maxima and minima (circles in Fig. 1d, f). More intercomparison is provided in the methods.

In summary, the present pattern continuum representation can characterize major ENSO spatial features (diversity, asymmetry) with respect to spatial shifting intensity[4,5,8]. Individual sample correspondence is also reasonable overall. In the next section, we interpret these continuums in the view of truncated SST variations, in which spatial shifting approximately conserves geometrical structures.

Shifted mean flow

Here, we propose a truncation called "shifted-mean flow" that enables interpreting spatial shifting more simply in the SST data. As discussed above, the SST structure (of warm pool, cold tongue) tends to shift as a whole with WPEP (Fig. 1a). A relevant approximation (or null hypothesis) is to consider that the structure is conserved along the movement, as in TD23. Consider again the observed total SST $T(x, t)$ in the equatorial Pacific, where x is longitude and t is time, as well as the WPEP $\chi(t) = \overline{\chi} + \chi'(t)$ with temporal mean $\overline{\chi}$ and anomalies $\chi'(t)$. We want to check the relation $T(x, t) \approx S[x - \chi'(t)]$, where $S(x)$ is a constant profile whose shift would describe the dynamics of T. This can be transformed into the relation $S(d) \approx T[d + \chi'(t), t]$, with new variables d and t, and if the present approximation is true, it must hold for temporal averaging as $S(d) \approx \overline{T[d + \chi'(t)]}$. Thus, we define a SST shifted-mean flow as $\widetilde{T}(x, t) = S[x - \chi'(t)]$, where $S(x) = \overline{T[x + \chi'(t), t]}$ is a temporal average of the flow relative to the moving WPEP (Fig. 2). While $\widetilde{T}(x, t)$ is defined over the equatorial Pacific, $S(x)$ is unbounded. The flow $\widetilde{T}(x, t)$ is directly estimated from $T(x, t)$, and can be seen as a truncation of it (see "Methods" section). It consists simply of a constant structure moving zonally with WPEP (Fig. 2a, d), which is a strongly nonlinear yet univariate process (once S is determined, it only depends on χ'). A shifted-mean SSTA flow is then deduced as $\widetilde{T}'(x, t) = \widetilde{T}(x, t) - \overline{\widetilde{T}(x, t)}$, and its variations are comparatively less trivial (Fig. 2b, c, e). The present formulation shares similarities with TD23[10] (see "Methods" section) and previous models from the literature[15].

If our approximation of an SST structure (S) being conserved along the movement is relevant, then $\widetilde{T} \approx T$ (or $\widetilde{T}' \approx T'$). The shifted mean flow, in fact, compares quite well with the observed flow on smoothed pattern continuums (Fig. 1e, f vs Fig. 2a, b). Here, T and $\widetilde{T}$ are visually similar, and $\widetilde{T}'$ retrieves both the pattern diversity and asymmetry of T'. The main discrepancies, albeit slight, are a weaker CP cooling around the 0th quantile and a weaker EP warming around the 90th quantile. We may also compare $\widetilde{T}$ directly to the full (unsmoothed) version of T, for which we find, as in the previous section, that the comparison is reasonable overall but non-systematic (e.g., Figs. 1b, d vs 2b, c as ordered by increasing WPEP or by increasing time). As one example, unsmoothed El Niños in $\widetilde{T}$ peak just west of the WPEP, while strong La Niñas peak around 160° W, which is the overall behavior from T (circles in Figs. 2b vs 1f). More intercomparison is provided in the methods.

The advantage of the present shifted-mean flow is that it allows interpreting SST fluctuations from spatial shifting in a simplified way. As discussed in the previous section, the gradual transitions on the SSTA smoothed pattern continuum support the notion that ENSO diversity organizes into a continuum rather than distinct event types[5,21,22] (Fig. 1f). Within the view of the simplified shifted-mean flow, we can interpret this continuum by analyzing gradual changes in spatial shifting intensity. Let $\chi'(t)$ be varied gradually, then $\widetilde{T}(x, t) = S[x - \chi'(t)]$ generates a continuum of translated SST patterns (Fig. 2d, e). Consider now, for simplicity that $\overline{\widetilde{T}}(x, t) \approx S(x)$, that is the mean state is approximately retrieved when the WPEP is at its resting position $\chi'(t) = 0$. This leads to

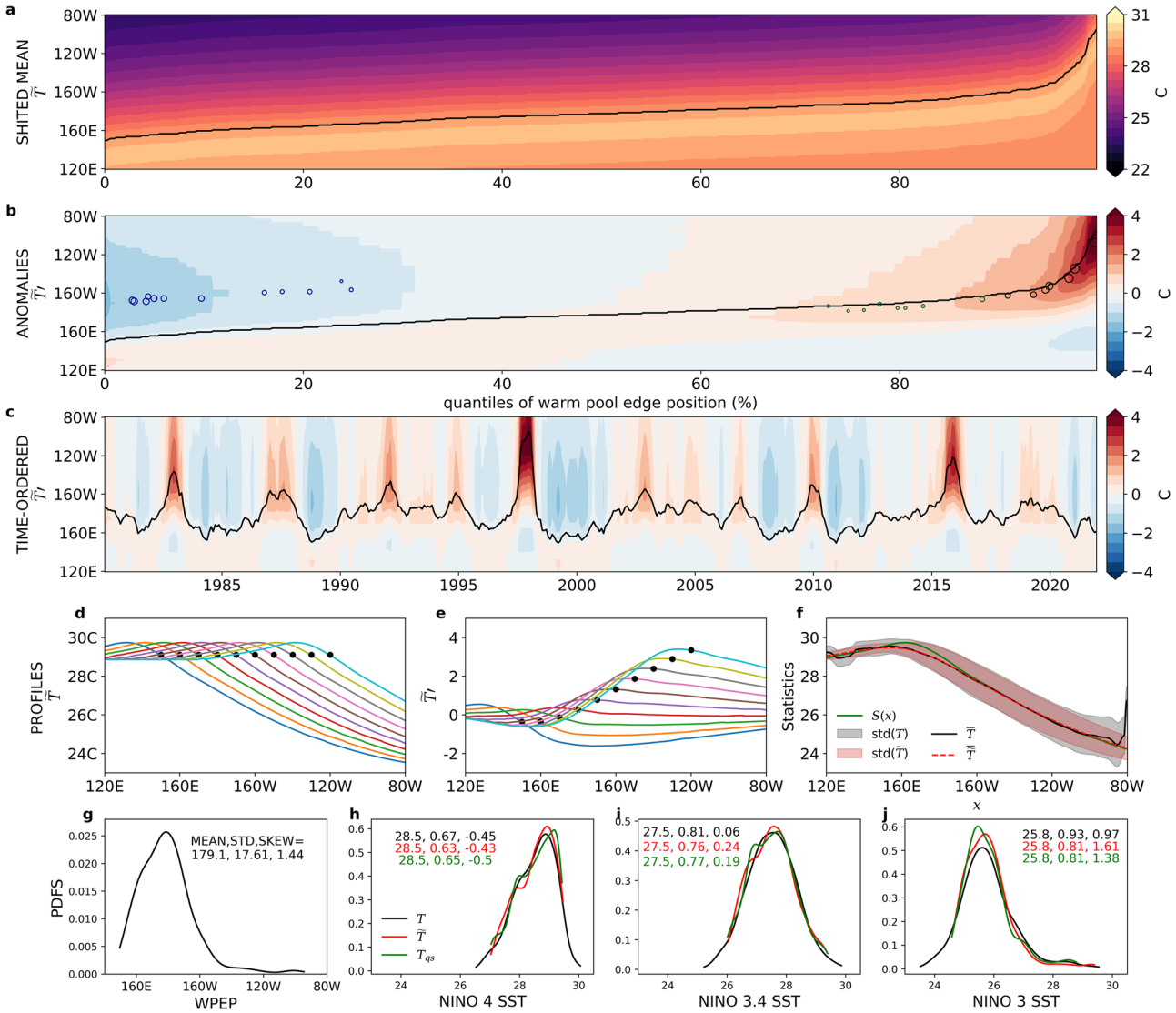

Fig. 2 | Shifted-mean SST flow. a Shifted-mean SST flow $\widetilde{T}(x,t) = S[x - \chi'(t)]$, quantile-ordered with WPEP $\chi(t)$ as in Fig. 1 but not smoothed (as $\widetilde{T}$ already varies smoothly with WPEP). The black line indicates WPEP. **b** Same as a for the shifted-mean SSTA flow $\widetilde{T}'(x,t) = \widetilde{T}(x,t) - \overline{\widetilde{T}}(x,t)$. Individual ENSO event peaks are indicated (circles as in Fig. 1f). **c** Hovmoller of $\widetilde{T}'$(x,t) as a function of time and longitude. **d** SST profiles $S(x-u)$ obtained by varying an arbitrary u in 10-degree increments, which translates the profile. Black dots indicate WPEP. **e** As in d but for SSTA, i.e., we plot $S(x-u) - \overline{\widetilde{T}(x,t)}$. **f** SST Profile $S(x)$, as well as mean and standard deviation intercompared between T and $\widetilde{T}$. We verify $\overline{\widetilde{T}(x,t)} \approx S(x)$. **g–j** Probability density functions (smoothed) for WPEP and total SST averaged in each Niño region, as intercompared between flows T, $\widetilde{T}$ and T_{qs} (where T_{qs} is the quantile-smoothed SST from Fig. 1f, see "Methods" section). Labels indicate mean, standard deviation, and skewness.

$\widetilde{T}'(x,t) \approx S[x - \chi'(t)] - S(x)$, meaning we can interpret ENSO SSTA patterns simply as the differences between a shifted structure and itself at rest, for a given spatial shifting intensity $\chi'(t)$. In Fig. 2b, starting from the resting position $\chi'(t) = 0$ around the 50th quantile, a gradual, more intense spatial shifting $\chi'(t) > 0$ or $\chi'(t) < 0$ generates gradually more intense differences at high and low quantiles, resulting in a centered continuum in pattern intensity. However, because differences are geometrical, they vary nonlinearly with $\chi'(t)$, leading to non-trivial pattern diversity within the continuum: a westward La Niña shifting pattern $\chi'(t) < 0$ (low quantiles), for example, is not the symmetric of an El Niño eastward shifting pattern $\chi'(t) > 0$ (high quantiles), and a moderate CP shifting pattern does not scale linearly into an intense EP shifting pattern. This mimics the overall ENSO pattern diversity and asymmetry in nature.

As regards detailed statistics, $\widetilde{T}$ captures the mean and standard deviation of (unsmoothed) T despite discrepancies near ocean borders (Fig. 2f), and we verify $\overline{\widetilde{T}(x,t)} \approx S(x)$. Importantly, $\widetilde{T}$ captures the non-Gaussian statistics[33,34] of T in each Niño region (Fig. 2h,i,j). In T, Niño 3 SST (and to a lesser extent Niño 3.4 SST) is positively skewed while Niño 4 SST is negatively skewed, which is commonly believed to arise from dynamical nonlinearity[35–37]. Here, we can relate this skewness more simply to the basic geometrical nonlinearity of $\widetilde{T}(x,t) = S[x - \chi'(t)]$[15]. Assuming, for example $\chi'(t)$ small and $S[x - \chi'(t)] \approx S(x) - \chi'(t)\dot{S}(x)$, then a positively skewed WPEP distribution (Fig. 2g) leads to SST skewness that is positive in the east ($\dot{S} < 0$) and negative in the center-west ($\dot{S} > 0$).

In summary, the present shifted-mean flow, in which a fixed structure shifts conservatively, truncates the observed SST flow and approximates it reasonably well, most strikingly its pattern continuum and non-Gaussian statistics. With this truncation, we can interpret ENSO SSTA patterns as emerging from gradually increasing differences between a shifting SST structure and itself at rest, which also generates pattern diversity, asymmetry, and a smooth

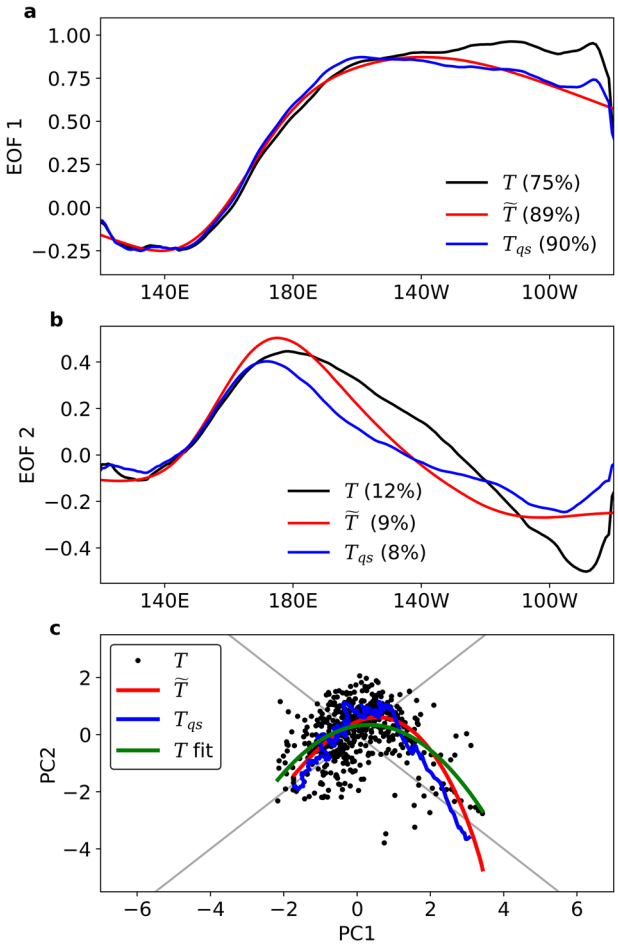

Fig. 3 | Principal component analysis. a First EOF (E_1) as deduced from either SST T (black), shifted-mean SST flow $\widetilde{T}$ (red), or quantile-smoothed SST T_{qs} (blue). Explained variance is indicated in %. **b** As in a but for the Second EOF (E_2). **c** Scatterplot between PC1 (p_1) and PC2 (p_2) for T (black), $\widetilde{T}$ (red), and T_{qs} (blue). For T, we further indicate a quadratic fit (green line).

continuum[5,21,22]. In the next section, we investigate more implications of this rationale.

Principal components

In this section, we contrast our pattern continuum and shifted-mean flow diagnosis with principal component analysis (PCA) of SSTA. We interpret in particular the quadratic relationship between principal components[24,26] that is now widely used as a metric of ENSO non-linearity in data and models[22,38–40]. Given a flow $F(x, t)$, PCA is a linear projection:

$$F(x,t) = \sum_{i=1}^{N} R_i(x,t) + \overline{F}(x), \text{ with } R_i(x,t) = E_i(x)p_i(t) \qquad (1)$$

where E_i are empirical orthogonal functions (EOFs), p_i are principal components (PCs), ordered by decreasing explained variance, and N is the size of x[41]. Truncated flows with reduced dimensionality $n \le N$ may recover most important variations, e.g., $n = 2$ reasonably captures ENSO variations in equatorial SST[24,26].

Taking $n = 2$, in Fig. 3 we intercompare PCA for F being either the SST flow T (Fig. 1a, c), the shifted-mean SST flow $\widetilde{T}$ (Fig. 2a), or the quantile-smoothed SST from Fig. 1e denoted hereafter T_{qs} (see "Methods" section). There is a good agreement between PCA of each flow overall, even though $\widetilde{T}$ underestimates EP variations on E_1 (also leading non-trivially to discrepancies on E_2). There is approximately a quadratic relationship between p_1 and p_2 (Fig. 3c), which is fundamental for ENSO nonlinear dynamics but not fully understood[22,38,39]. Our simplified shifted-mean flow $\widetilde{T}$ captures this relationship overall. Recall $\widetilde{T}$ is univariate, which is why its p_1 vs p_2 scatterplot is a single line (as is also approximately the case for T_{qs}).

Because $\widetilde{T}$ is univariate, we can use it to interpret more simply the mechanisms of PCA decomposition, including the emergence of the quadratic relationship. Despite being univariate, $\widetilde{T}(x,t) = S[x - \chi'(t)]$ is nonlinear in both space and time, thus it cannot project linearly on a single PC. Thus, it projects on at least two PCs as $\widetilde{T}'(x,t) \approx R_1(x,t) + R_2(x,t)$ (Fig. 4a, b), where we recall $R_1(x,t) = E_1(x)p_1(t)$, $R_2(x,t) = E_2(x)p_2(t)$. Considering $\overline{\widetilde{T}(x,t)} \approx S(x)$ as in the previous section, we can also denote the PCA more compactly as $S[x - \chi'(t)] - S(x) \approx p_1(t)E_1(x) + p_2(t)E_2(x)$. From this, we see that p_1 and p_2 depend solely on χ' i.e., on the spatial movement. In fact, p_1 increases roughly linearly with χ' while p_2 is roughly quadratic in χ' (Fig. 4e), and thus p_1, p_2 are themselves tied quadratically. Importantly, the dependencies of p_1 and p_2 on χ' emerge from how E_1, E_2 (or equivalently R_1, R_2) combine spatially to reconstruct $S[x - \chi'(t)] - S(x)$, which involves grasping the geometry of the SSTA pattern continuum in Fig. 4a. Neither R_1 nor R_2 alone can capture all SSTA patterns because they have fixed spatial structures (Fig. 4c, d). When summed, however, the dipole pattern of R_2 may shift eastward or westward the broad warming/cooling pattern of R_1: this happens at low quantiles ($p_1, p_2 < 0, \chi' < 0$) giving central La Niña, and at high quantiles ($p_1 > 0, p_2 < 0, \chi' > 0$) giving EP El Niño. At medium-high quantiles ($p_1 \approx >0$, $p_2 > 0, \chi' \approx >0$), R_2 dominates giving CP El Niño (Fig. 4b). From this we retrieve the roughly linear(quadratic) dependency of $p_1(p_2)$ on χ'. Although $\widetilde{T}$ is a simple flow, the present intuition is rather similar to the PCA decomposition of observed SST T (see "Methods" section).

In summary, approximating ENSO SST variability as a shifted-mean flow (in which a fixed structure shifts conservatively) helps interpret the PCA. The univariate but nonlinear flow necessarily projects on two PCs that are tied quadratically, and this quadratic dependency stems from how two fixed spatial structures (the EOFs) combine to grasp the continuum of SSTA patterns associated with spatial shifting.

Discussion

In this paper, we have implemented a series of diagnostics to quantify ENSO spatial shifting in SST observations in the equatorial band (GODAS reanalysis[23], averages 5° N–5° S with seasonality omitted). A pattern continuum representation, which consists of ordering SST maps into WPEP quantiles, grasps major ENSO features (pattern diversity and asymmetry). It can be effectively approximated by a nonlinear and univariate shifted-mean flow where a constant structure is moved zonally. Finally, the shifted-mean flow helps interpret the quadratic relationship of SST PCA.

The present results provide observational evidence that supports the intuition of the theoretical ENSO model from TD23[10]. While in TD23 an idealized shifted-mean SST flow was used, we use here a shifted-mean flow deduced from data, which improves realism and consistency. The conclusions nevertheless remain similar, that spatial shifting shapes ENSO variability in a major way. ENSO pattern diversity in SSTA, for example, can here be interpreted from the gradual shifting of an approximately conserved structure (the Walker circulation) with respect to itself, which generates geometrically a non-trivial continuum of patterns[5,21,22]. The same process also generates pattern nonlinearity and asymmetry. The present hypothesis is, of course, up for debate and should be reconciled with existing literature[17]. Theoretical models for ENSO diversity, in fact, usually depict the phenomena as being at least bivariate in SST and bimodal, with separate rather than unified dynamical processes driving the CP or EP types[37,42,43].

A main limitation of our approach is that some SST variations are unaccounted for in the far EP. Intuitively, this is because of border reflections (e.g., of equatorial Kelvin waves into equatorial Rossby waves[27]) that necessarily alter the SST structure shifting zonally, as well as locally induced SST variations that are more a consequence than a driver of basin-scale adjustment (e.g., Coastal El Niños[28]). This deserves further investigation. Another limitation is that interactions with seasonality are unaccounted for[31]: for example, the SST gradient over the cold tongue varies with seasons,

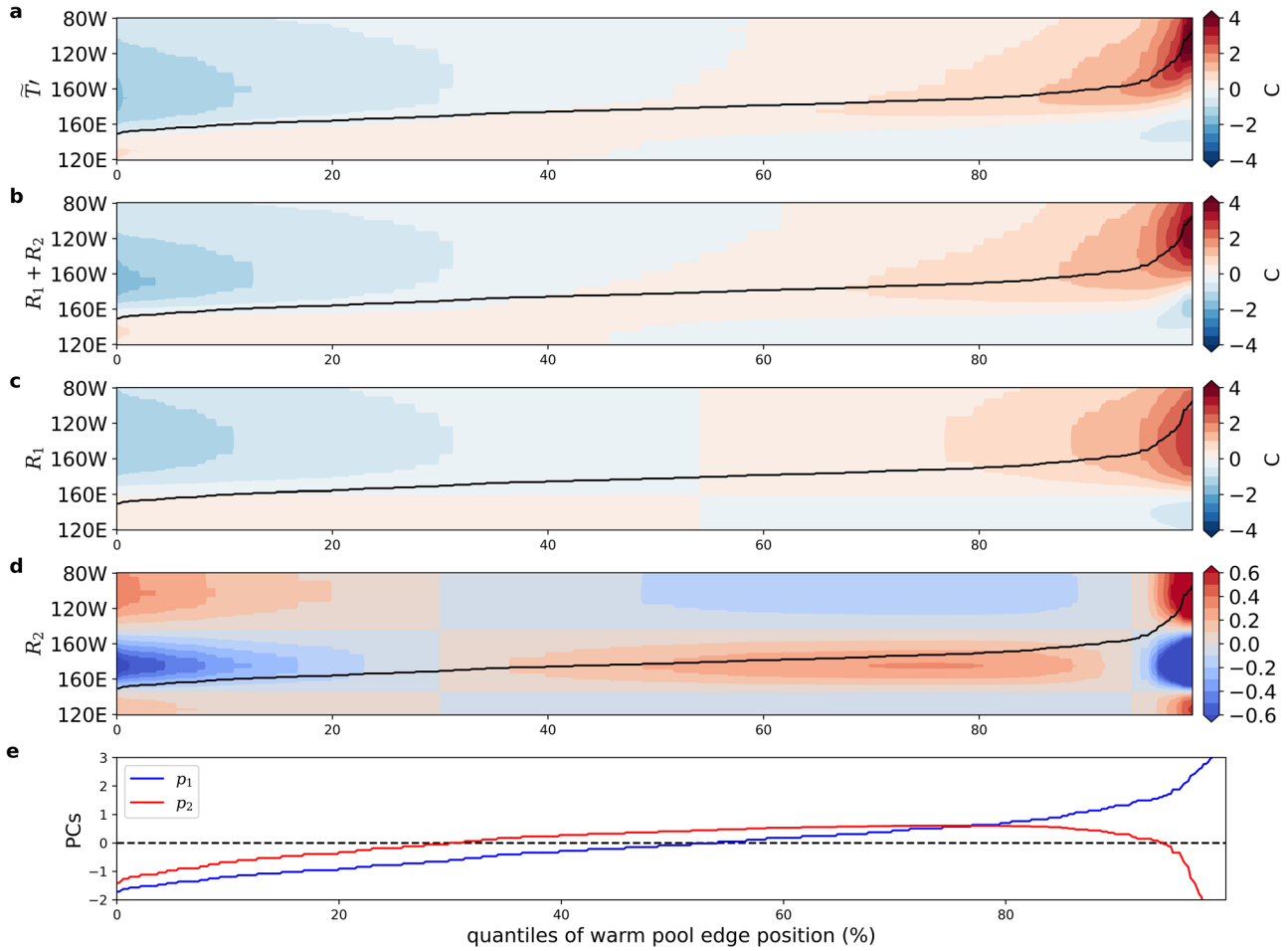

Fig. 4 | Pattern continuum of $\widetilde{T}'$ and its PCA. a Pattern continuum of shifted-mean SSTA flow $\widetilde{T}'$, quantile-ordered with WPEP but not smoothed. WPEP is indicated (black line). **b** Same as a for $R_1 + R_2$ as deduced from PCA of $\widetilde{T}'$. **c** Same as a for $R_1 = E_1 p_1$. **d** Same as a for $R_2 = E_2 p_2$. **e** Principal components p_1,p_2 ordered into quantiles of WPEP.

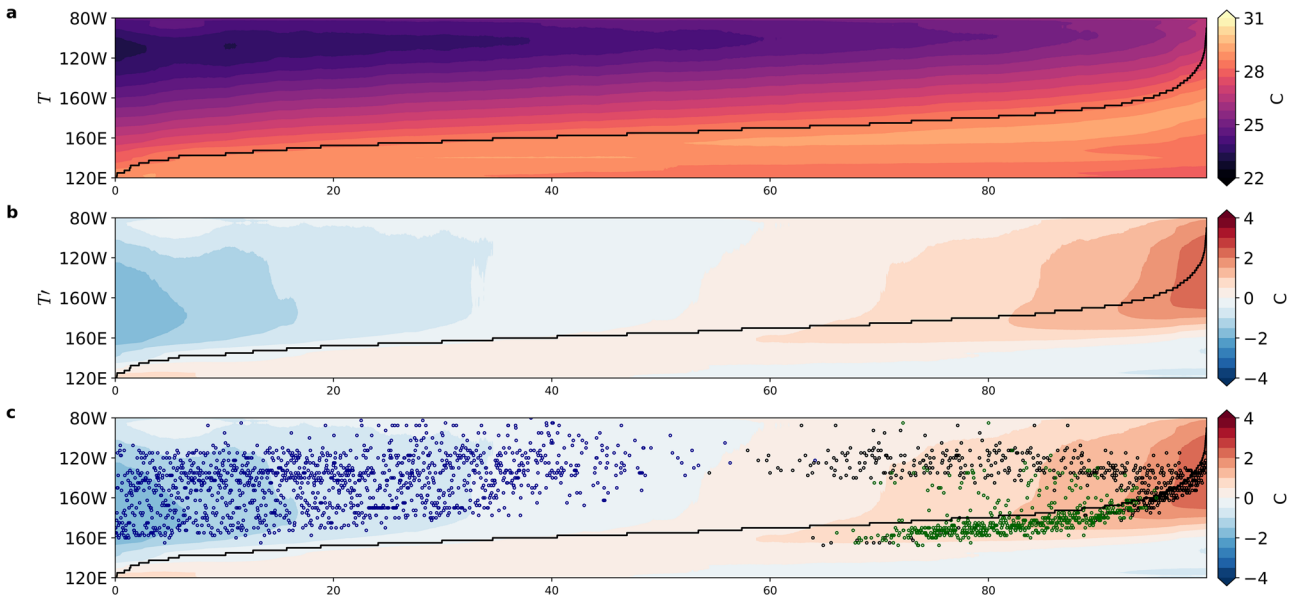

Fig. 5 | Pattern continuum of CESM-LE SST. a SST from CESM-LE ordered by increasing quantiles of WPEP (in %), as in Fig. 1e, but smoothed here with a running-mean of 2150 samples. WPEP is indicated (black line). **b** Same as a but for SSTA. **c** Same as (**b**), but overplotting the position of individual ENSO events peak warming/cooling (circle color: blue for La Niña, green for CP El Niño, and black for Eastern Pacific El Niño, there is no indication of event intensity).

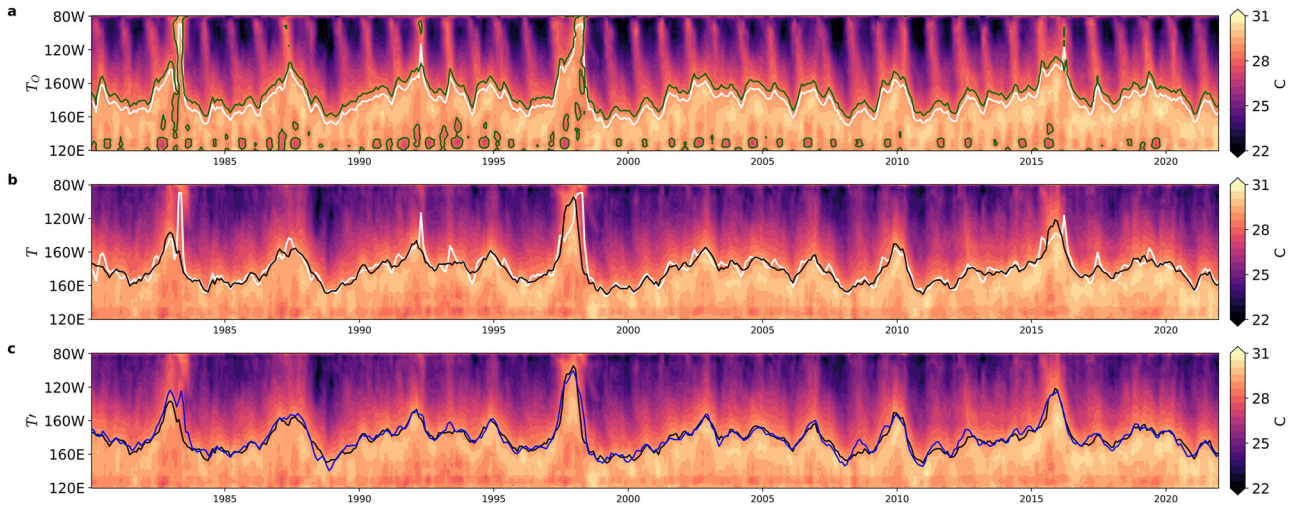

Fig. 6 | WPEP estimation. a Hovmoller of total SST with seasonal variations (T_O), averaged 5° N–5° S, as a function of time t (years) and longitude x (deg E), with directly estimated WPEP (white line) and 28.5 °C isotherm (green line). **b** Total SST $T(x, t)$ (without seasonal variations) and its estimated WPEP (black line). WPEP from (**a**) is repeated (white line). **c** Total $T(x, t)$ as in (**b**) with WPEP from (**b**) repeated (black line), also showing an optimized WPEP $\chi_g(t)$ (blue line, see text). $\chi(t)$ is estimated in the present paper as the black line in (**b**, **c**).

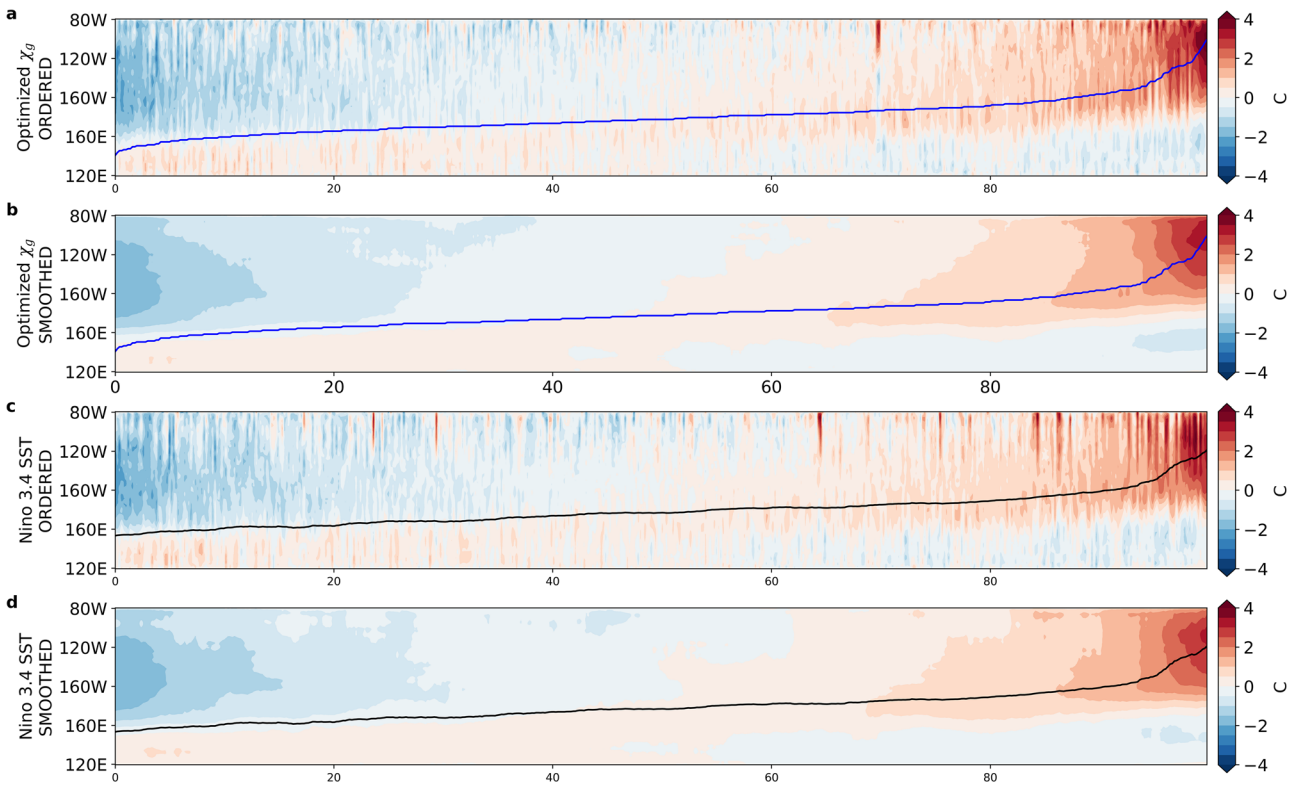

Fig. 7 | Alternative metrics for spatial shifting intensity. a SSTA T' ordered in quantiles of an optimized WPEP χ_g (blue line, see text). **b** Same as a but smoothed. **c** SSTA T' ordered in quantiles of Niño 3.4 SST. **d** Same as c but smoothed. χ_g or Niño 3.4 SST may also be considered to indirectly measure spatial shifting.

which should modify the shifted-mean profile (see "Methods" section). Meridional dependency should be considered as well[29,30,32,44].

Beyond this, perspectives on investigating the role of spatial shifting are rather broad, e.g., as regards ENSO modeling with hierarchical complexity[17,45,46] (where spatial shifting nonlinearity can be easily integrated), ENSO teleconnections (as Walker circulations are interconnected over the equatorial belt[1,47,48]), decadal variability and climate change[39,40,49] (as spatial shifting modifies the mean flow nonlinearly[15]), and so on. In fact, because the spatial shifting intuition is very elementary, it may apply to a broad range of issues. One direct perspective of this work is to apply the present diagnosis to other fields representative of ENSO variability (e.g., zonal wind stress, thermocline depth, etc), because the Walker circulation tends to shift as a whole[10].

The present diagnosis (pattern continuum and shifted-mean approximation of a given flow) may be useful for quantifying other SST datasets, including simulations from general circulation models. In fact, we acknowledge that results may differ on other datasets (including reanalysis), which should be investigated. As a brief consistency check, we have repeated our analysis in two SST reconstruction datasets (see "Methods" section). As another brief example, we

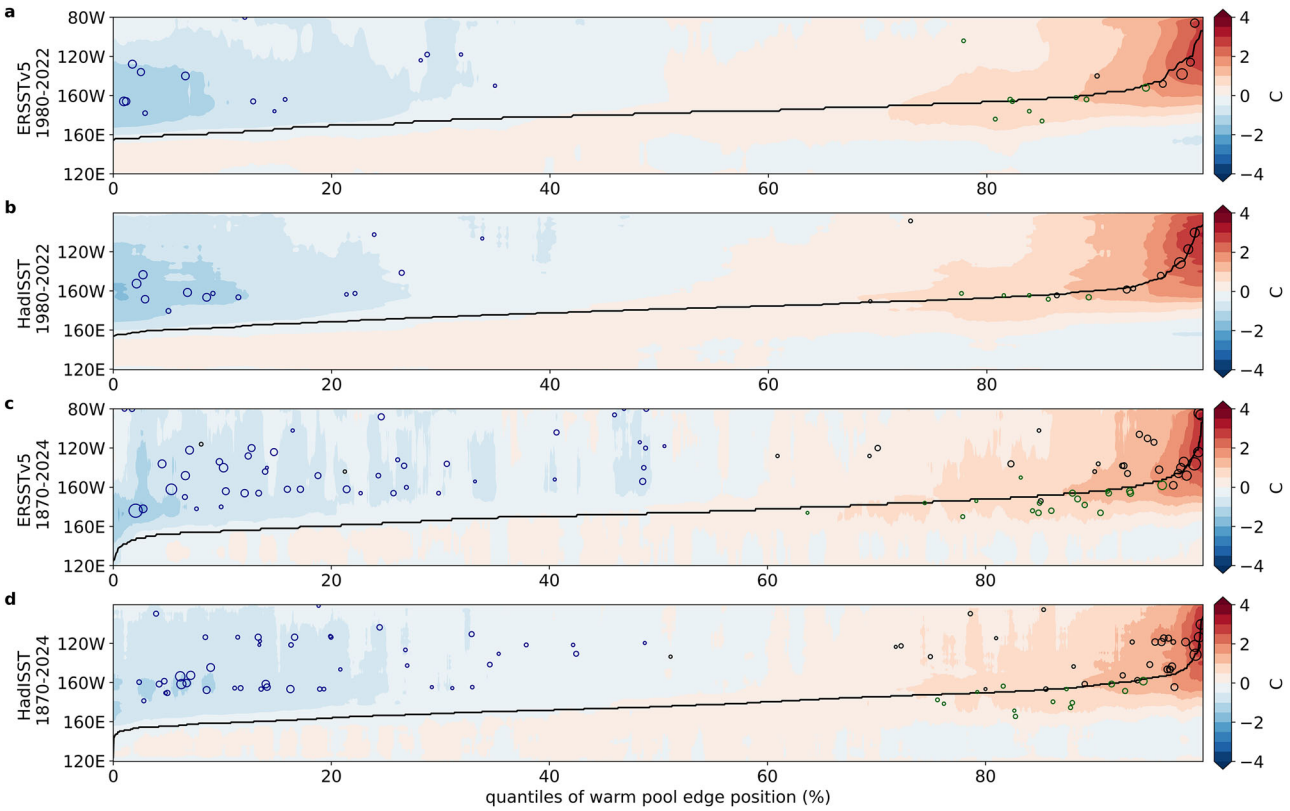

Fig. 8 | Pattern continuums in other SST products. a Pattern continuum of SSTA computed from ERSSTv5 over 1980–2022. The black line indicates WPEP, and circles indicate ENSO event types and amplitude. See Fig. 1f (GODAS over 1980–2022) for comparison. **b** Same for HadISST 1980–2022. **c** Same for ERSSTv5 1870–2024. **d** Same for HadISST 1870–2024. For (**c**, **d**) smoothing uses a running mean of 89 samples, and WPEP uses an additional correction (see text).

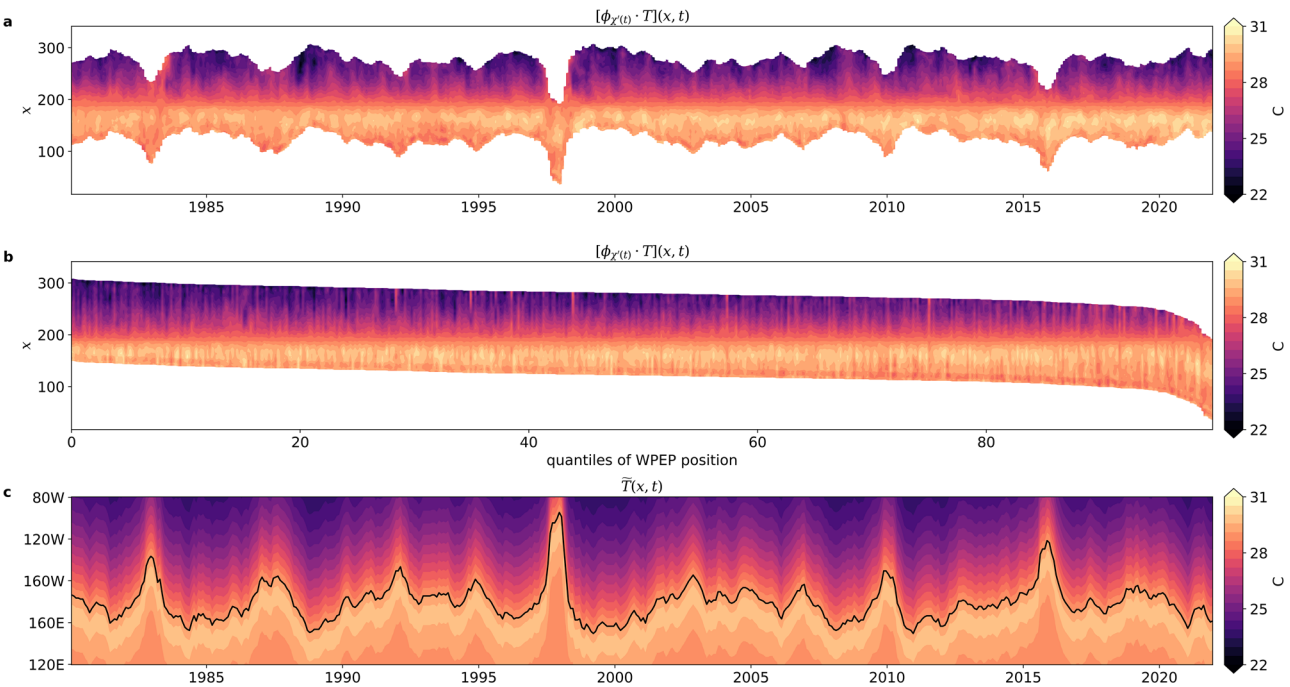

Fig. 9 | Shifted-mean SST flow formulation. a Hovmoller of SST centered on WPEP, i.e. $[\phi_{\chi'(t)} \cdot T](x,t) = T[x + \chi'(t), t]$, as a function of time and position x (deg E). White areas are out of bounds (with $x + \chi'(t)$ outside of the equatorial Pacific 120° E–80° W). Centered SST within bounds is roughly constant with time. **b** Same as a but reordered by quantiles of WPEP. With this representation, it is even clearer that centered SST is roughly constant with time, thus approximable by $S(x) = \overline{[\phi_{\chi'(t)} \cdot T](x,t)}$ (omitting out-of-bounds areas in the averaging). **c** Hovmoller of shifted mean SST flow $\widetilde{T}(x,t) = [\phi_{-\chi'(t)} \cdot S](x,t) = S[x - \chi'(t)]$.

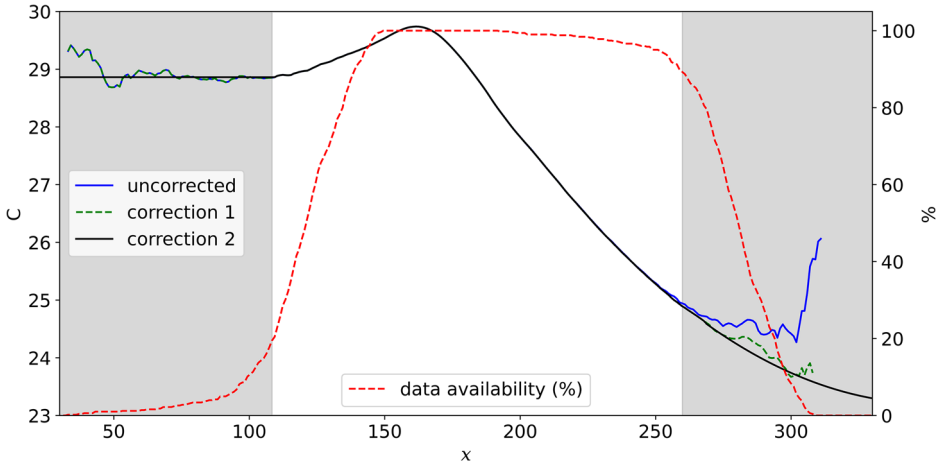

Fig. 10 | Corrections to the Shifted-Mean SST profile *S*. Initial shifted-mean profile (blue), first correction omitting eastern border data (green dashed), and second correction smoothing the profile at edges (plain black), as a function of position x (deg E). Gray areas indicate equatorial Pacific edges (120° E, 80° W). There is limited data availability around edges (% of record where $x + \chi'(t)$ is within 120° E–80° W, red-dashed).

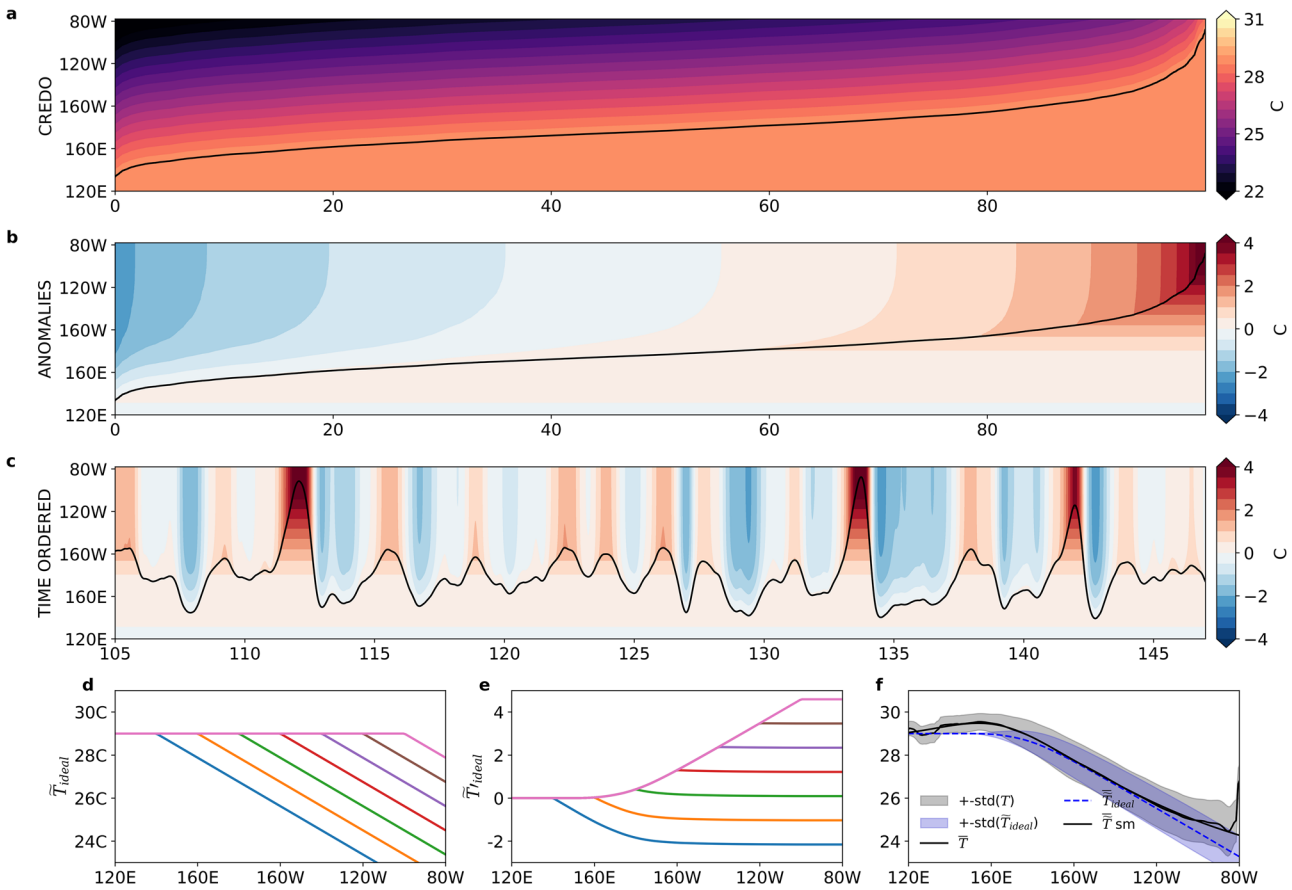

Fig. 11 | Idealized shifted-mean flow $\widetilde{T}_{ideal}$. a Shifted-Mean Flow $\widetilde{T}_{ideal} = S_{ideal}[x - \chi'(t)]$, quantile ordered with WPEP but not smoothed. Here, χ is obtained from the integration of the conceptual model from TD23. **b** Same as a, but for anomalies $\widetilde{T}'_{ideal}$. **c** Hovmoller of $\widetilde{T}'_{ideal}$, as a function of simulation time (years) and longitude. **d** SST profiles $S_{ideal}(x - u)$ obtained by varying an arbitrary u in increments of 20° as a function of longitude. **e** same as a for SSTA, i.e. we plot $S_{ideal}(x - u) - \overline{\widetilde{T}}_{ideal}$. **f** Mean and standard deviation intercompared between true SST flow T and $\widetilde{T}_{ideal}$.

have computed the pattern continuum of SST resulting from long-term simulation of the general circulation model CESM-LE[50,51] (Fig. 5). Such a simulation is invaluable due to its large sampling that increases statistical confidence as well as its ability to capture both CP and EP El Niños, among others[52] (see "Methods" section). The CESM-LE pattern continuum is comparable to our results yet deformed (Fig. 5b vs Fig. 1f). Looking at individual event peaks, most CP (and some EPs) El Niños peak just west of WPEP, while La Niñas peak in the CP, as in our results (Fig. 5c). However, in CESM-LE, there are a multitude more of EP El Niño events peaking around 120° W–140° W in the 60th–90th quantile range, making EP and CP events very distinct (and pointing towards a bivariate-bimodal variability). La Niñas also exhibit a slight preference for the 120° W–140° W range. These discrepancies may point toward a CESM-LE model bias, but it is also possible that CESM-LE is closer to the true ENSO flow than our observations as statistical confidence is increased, which deserves further investigation. This at least shows the relevance of our diagnosis for model evaluation and intercomparison.

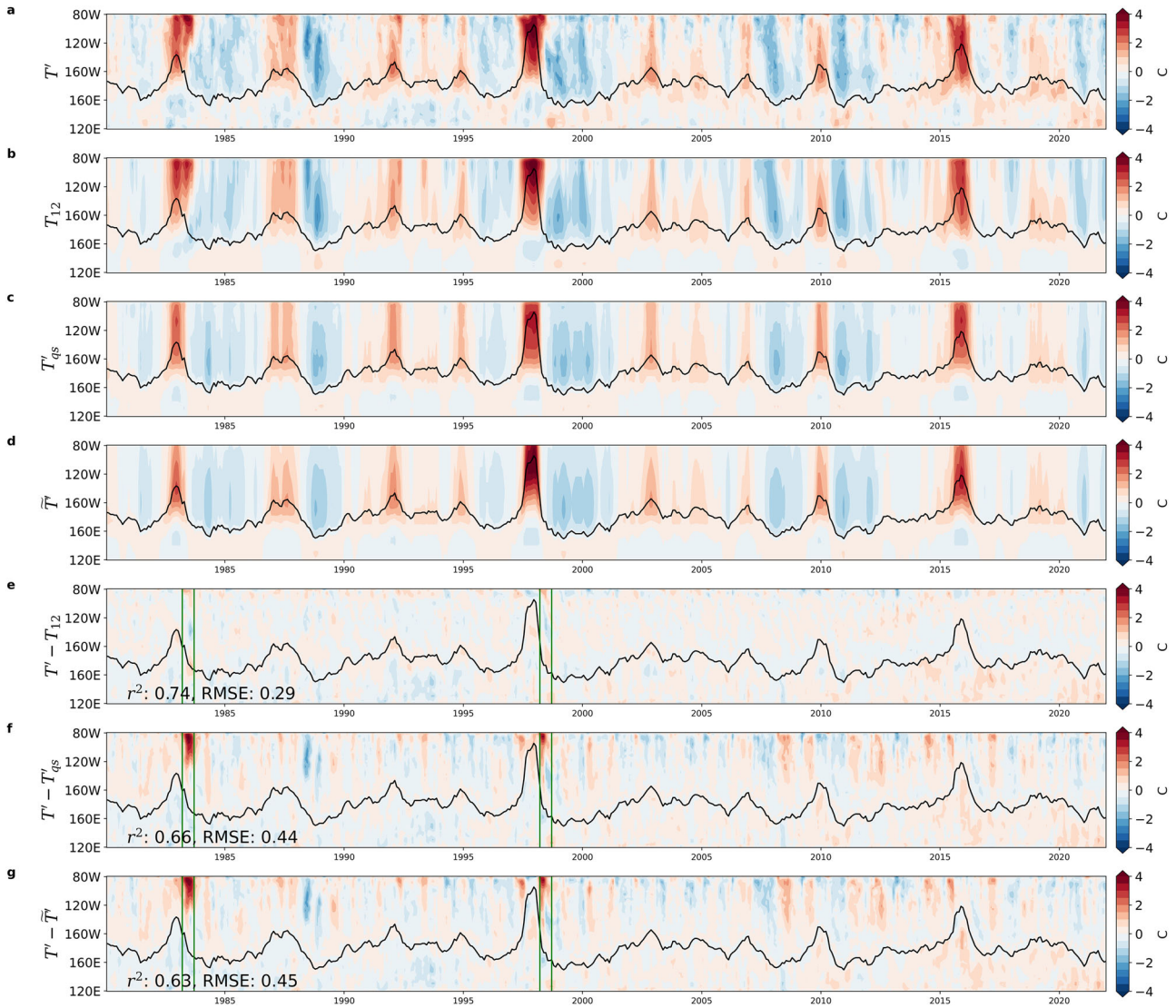

Fig. 12 | Reconstruction errors. a Observed SSTA flow $T' = T - \overline{T}$, as a function of time and longitude. **b** T'_{12} the PCA truncation of T'. **c** quantile-Smoothed SSTA flow T'_{qs}. **d** Shifted Mean SSTA Flow $\widetilde{T}'$. **e** Difference $T' - T'_{12}$ i.e., panels **a, b**. **f** Difference $T' - T'_{qs}$ i.e., panels **a**-**c**. **g** Difference $T' - \widetilde{T}'$ i.e., panels **a**-**d**. For panels **e**-**g**, we indicate the coefficient of determination r^2 and RMSE in reconstructing the "true" flow T' ($r^2 = 1$, RMSE = 0 for a perfect reconstruction).

Methods

Data sources

Observational SST data used in this paper are from the NCEP Global Ocean Data Assimilation System (GODAS[23]). Data is monthly over 1980–2022. In the discussion section, we also analyze SST from the 42 members of the historical simulations over 1920–2005 of the NCAR Community Earth System Model Large Ensemble Project (CESM-LE)[50–52]. To overcome the model's cold bias[51], WPEP in CESM-LE is measured for a target warm pool saturation SST of 28.5 °C (instead of 29 °C, see below). Hereafter, in the methods section, we also briefly analyze two SST reconstruction datasets, respectively NOAA Extended Reconstructed SST V5 (ERSSTv5) and Hadley Centre Global Sea Ice and SST V1.1 (HadISST)[53,54]. For these two datasets, we consider data either over 1980-2022 (for direct comparison with GODAS) or over 1870–2024. Meridional averaging is 5° N–5° S by default but slightly adapted to each dataset grid: 5° N–5° S in GODAS and CESM-LE, 6° N–6° S in ERSSTv5, and 5.5° N–5.5° S in HadISST. GODAS and ERSSTv5 are provided by the NOAA/OAR/ESRL PSL, Boulder, Colorado, USA, from their website. CESM-LE is provided by NSF/CISL/Yellowstone. HadISST is provided by the Met Office Hadley Centre.

Consider the SST observations T_O in the equatorial Pacific averaged 5° N–5° S, depending on longitude x (120° E–80° W) and time t (monthly). This decomposes generally as

$$T_O(x,t) = \overline{T}(x) + T_S(x,s) + T'(x,t) \tag{2}$$

where $\overline{T}$ is the mean, T_S the seasonal variations (depending on time of year s), and T' the anomalies. For simplicity, we omit the seasonal variations in the present paper i.e., we denote $T = T_O - T_S$ the "total" observed SST with a slight abuse of definition.

WPEP

The WPEP computation is as in TD23[10] and roughly similar to other computations beyond practical differences[11,13,14,22]. The WPEP roughly measures the 29°C isotherm, and is estimated as:

$$\chi(t) = L^{-1} \int_{x_W}^{x_E} \mathrm{bool}(\mathrm{T} > C_T) dx + \Delta_c \tag{3}$$

where T is total SST (with seasonal variations removed), the equatorial Pacific spans $x \in [x_W, x_E]$ (120° E–80° W) with length $L = x_E - x_W$, $C_T = 28.5$ °C is a threshold, the bool function maps 1 if the Boolean condition is true and zero otherwise, and $\Delta_c = -10$ °E is an empirical correction. In practice,

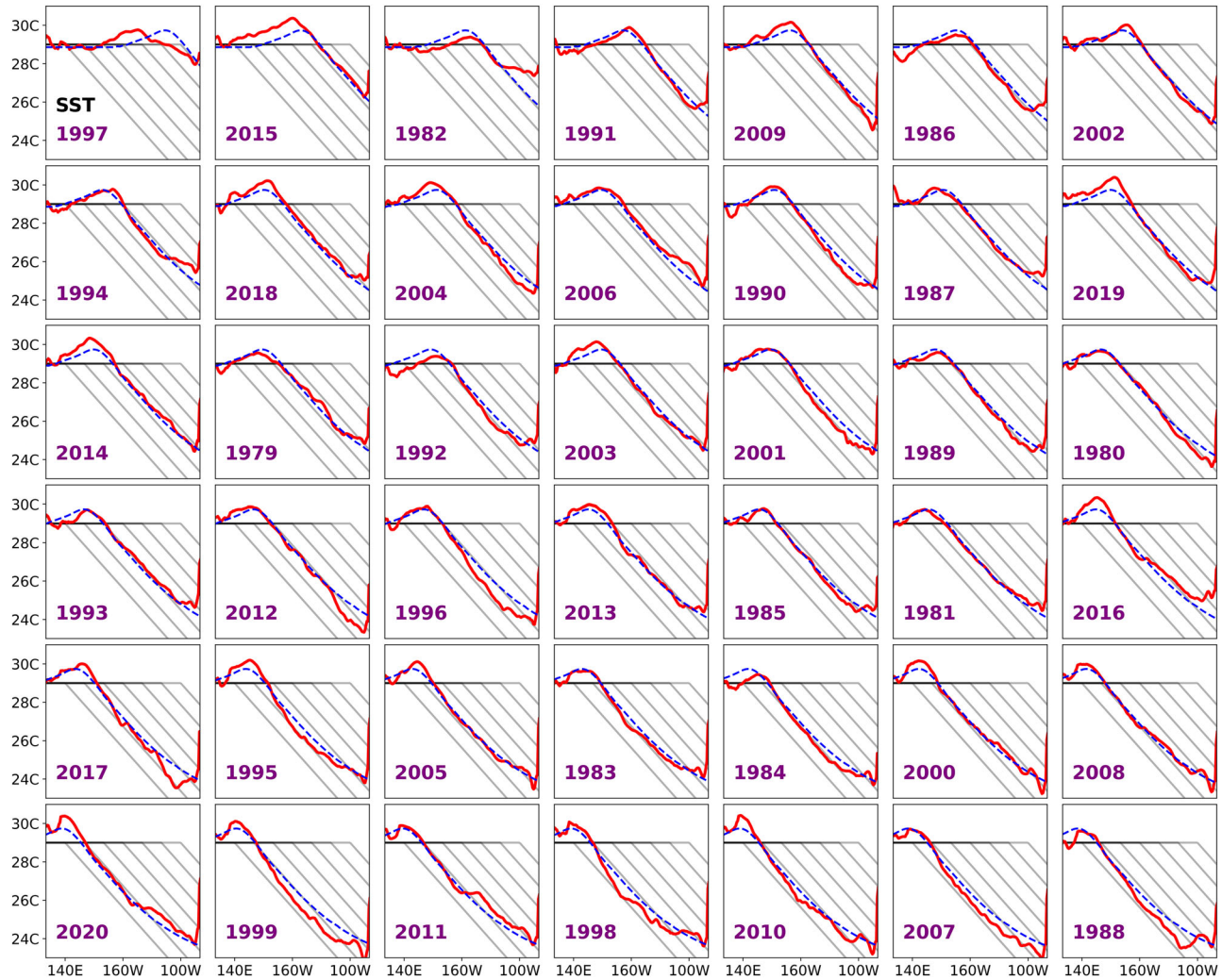

Fig. 13 | Individual SST profiles. SST profiles for individual ENSO events at their peak (DJF averages), with each panel a year within 1980–2022, ordered by decreasing WPEP (some years are neutral conditions). Intercompared for SST T (red) and shifted-mean SST flow $\widetilde{T}$ (blue dashed). Gray lines are arbitrary guidelines.

we compute χ once, set bool = 1 over the warm pool $x < \chi$, then recompute χ again. We also note $\chi = \overline{\chi} + \chi'$ the decomposition into mean and anomalies.

The present method empirically corrects a few issues associated with a direct estimation from the 28. 5 °C isotherm of seasonal SST[11] (Fig. 6a). First, the 28. 5 °C isotherm has additional contours due to occasional cooling in the far western Pacific: we are able to remove these thanks to the boolean threshold integration (computed twice). Second, the 28.5 °C isotherm actually coincides with the beginning of the cold tongue SST sloping, which is not strictly the edge of the warm pool area of saturating SSTs. For this reason, we empirically displace our measure by Δ_c such that χ corresponds visually to a 29 °C isotherm. Finally, in the present paper, we estimate WPEP from non-seasonal SSTs, leading to smoother variations (Fig. 6b). It is, however, unclear whether or not this estimate is most suitable right in the aftermath of 1982 and 1998, as it is in marked discrepancy with the seasonal estimate.

While we use here WPEP χ to measure spatial shifting intensity, other metrics may be considered as well. As one example, in Fig. 6c, we have estimated an "optimized" WPEP $\chi_g(t)$: for each time sample t, it is computed by minimizing RMSE (T(x, t), S[x − χ'_g]) (as averaged over longitude), i.e., by finding the optimal translation for which S aligns with the SST zonal profile. χ_g better captures the general movement than χ as it is less altered by local fluctuations around the 28.5 °C threshold, but its formulation is more complex. The SSTA pattern continuums recomputed with χ_g are in fact clearer, even without smoothing, with the exception of only one strong outlier that corresponds to mid-1983 (Fig. 7a, b). As another example, Fig. 7c, d shows an SSTA pattern continuum that is quantile-ordered and smoothed by increasing index Niño 3.4 SST (this index relates to WPEP roughly linearly, albeit slightly quadratically[10]). Results are similar overall, but the patterns are slightly less marked (and there are still individual sample discrepancies in the EP).

Comparison to SST reconstruction datasets

In order to assess the robustness of the paper's results, we briefly repeat them over two SST reconstruction datasets, ERSSTv5 and HadISST. Figure 8a, b shows the associated SSTA pattern continuums, computed over the same period 1980–2022 as GODAS. The overall features are consistently retrieved, including the gradual pattern transitions between ENSO types, the patterns' asymmetry, and the alignment of individual event peaks. Figure 8c, d shows the same pattern continuums recomputed over the extended record 1870–2024. Again, the results are consistent overall. For these experiments, we have added a small correction to WPEP: whenever $\chi(t) \leq 140$ °E, $\chi(t)$ is bad-valued and then refilled from neighboring values using spline interpolation. This adjustment corrects unrealistic WPEP values found in ERSSTv5 (but not in HadISST) prior to the 1960s, most likely due to data scarcity and resulting uncertainties in defining the warm pool. The impact of sampling uncertainty on WPEP estimates warrants investigation, but is beyond this paper's scope. Other features (shifted mean flows, SST statistics,

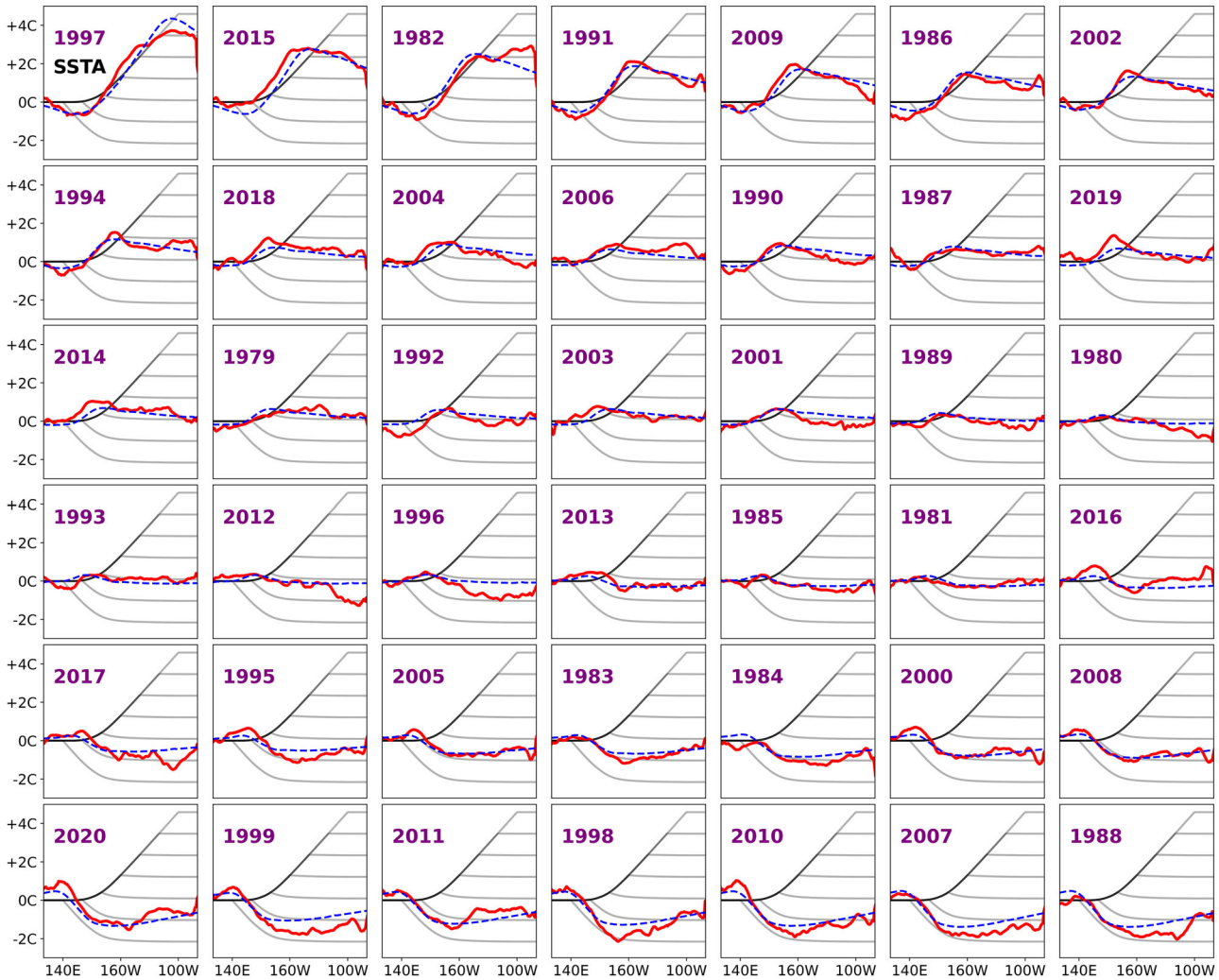

Fig. 14 | Individual SSTA profiles. Same as Fig. 13 but for SSTA.

PCA...) have also been briefly intercompared and found to be consistent overall across SST products and periods (not shown).

Shifted-mean flow formulation

We detail here the formulation of the shifted-mean flow $\widetilde{T}$. Consider again SST $T(x, t)$, as well as the WPEP $\chi(t)$ and its anomalies χ'.

We define the SST shifted-mean flow as $\widetilde{T}(x,t) = S[x - \chi'(t)]$, where $S(x) = \overline{T[x + \chi'(t), t]}$ (Fig. 2). As a more detailed derivation, consider a shift operator (or translation operator) ϕ_u, for $u \in \mathcal{R}$, applied to a function $f(x, t)$, by $[\phi_u \cdot f](x, t) = f(x + u, t)$. When applied to SST, as $[\phi_{\chi'(t)} \cdot T](x,t) = T[x + \chi'(t), t]$, we obtain data centered on the warm pool edge (Fig. 9a). Within the equatorial Pacific bounds, $[\phi_{\chi'(t)} \cdot T](x,t)$ is roughly constant with time (Fig. 9a, b), thus may be approximated by the shifted-mean profile $S(x) = \overline{[\phi_{\chi'(t)} \cdot T](x,t)} = \overline{T[x + \chi'(t), t]}$. The out-of-bounds data is ignored in this averaging, which leads to slight under-sampling issues at the extremities of S. Thus, a few minor corrections are made to S (see below).

Next, we build a shifted-mean flow by shifting back the profile with WPEP, which reads $\widetilde{T}(x,t) = [\phi_{-\chi'(t)} \cdot S](x,t) = S[x - \chi'(t)]$ (Fig. 9c). $\widetilde{T}$ is fundamentally nonlinear yet very simple mathematically, as we are just moving around a constant structure[15]. It is also univariate with a single degree of freedom χ'. Finally, we decompose the shifted mean into temporal mean and anomalies as $\widetilde{T}(x,t) = \overline{\widetilde{T}}(x) + \widetilde{T}'(x,t)$, where we denote $\widetilde{T}'$ hereafter as shifted-mean SSTA flow.

A few practical corrections are made to the shifted-mean SST profile S (Fig. 10). The Initial estimation isn't smooth at the extremities of S because of limited sampling. A first correction omits data $x > 277$. 5°E when averaging, which removes border effects. A second correction sets $S(x) = S(110°)$ for $x \le 110°$, and $S(x) = ax^2 + bx + c$ for $x \ge 270°$ with parameters estimated by polynomial fit over $x \in [200°, 270°]$. These practical corrections smooth the profile, and they also extend it, which allows dealing with potentially any amount of shifting.

Idealized shifted-mean flow

In TD23[10], the authors proposed an idealized shifted-mean SST flow:

$$\widetilde{T}_{ideal}(x,t) = T_W - \mathcal{H}(x - \chi)a(x - \chi) \tag{4}$$

where T_W, a are constants, and $\mathcal{H}$ is the Heaviside function. This flow also has the form $\widetilde{T}_{ideal}(x,t) = S_{ideal}[x - \chi'(t)]$. Figure 11 details flow characteristics, where χ is obtained from time integration of the model TD23. While $\widetilde{T}_{ideal}$ has the advantage of being idealized, it is less realistic than the data-derived flow $\widetilde{T}$. This can be seen e.g. on pattern continuums where La Niña cooling is too basin-wide and CP El Niño is less marked (Figs. 11b vs 2b), on general statistics (Figs. 11f vs 2f), or PCA (with explained variance of second PC that went from 3% in TD23 to 9% in Fig. 3b). Compared to $S_{ideal}(x)$, $S(x)$ includes a SST peak slightly west of the warm pool edge and a non-constant cooling rate over the cold tongue region (Figs. 11d vs 2d), which may explain some of the improvements.

Table 1 | Summary of main SST flows from the paper

Notation	T	T_{qs}	$\widetilde{T}$	T'_{12}	$\widetilde{T}'_{12}$
Flow name	Observed	Quantile Smoothed	Shifted Mean	T' PCA Truncation	$\widetilde{T}'$ PCA Truncation
Type	SST	SST	SST	SSTA	SSTA
Dependency	x, t	x, t	x, t	x, t	x, t
Dimension	Unknown	Unknown	1	2	1
Derivation method	average 5° N–5° S	quantile-smooth T w.r.t WPEP	$S = \overline{T(x+\chi', t)}, \widetilde{T} = S(x-\chi')$	Truncate T' to $R_1 + R_2$	Truncate $\widetilde{T}'$ to $R_1 + R_2$
Main features	ENSO + others	Spatial shifting	Spatial Shifting	Covariance main modes	Covariance main modes
Figures	1	1	2, 4	3	3, 4

The flows approximate the "true" SST flow T with the goal of grasping its ENSO variability. x is longitude (120° E–80° W), and t is monthly time (1980-2022).

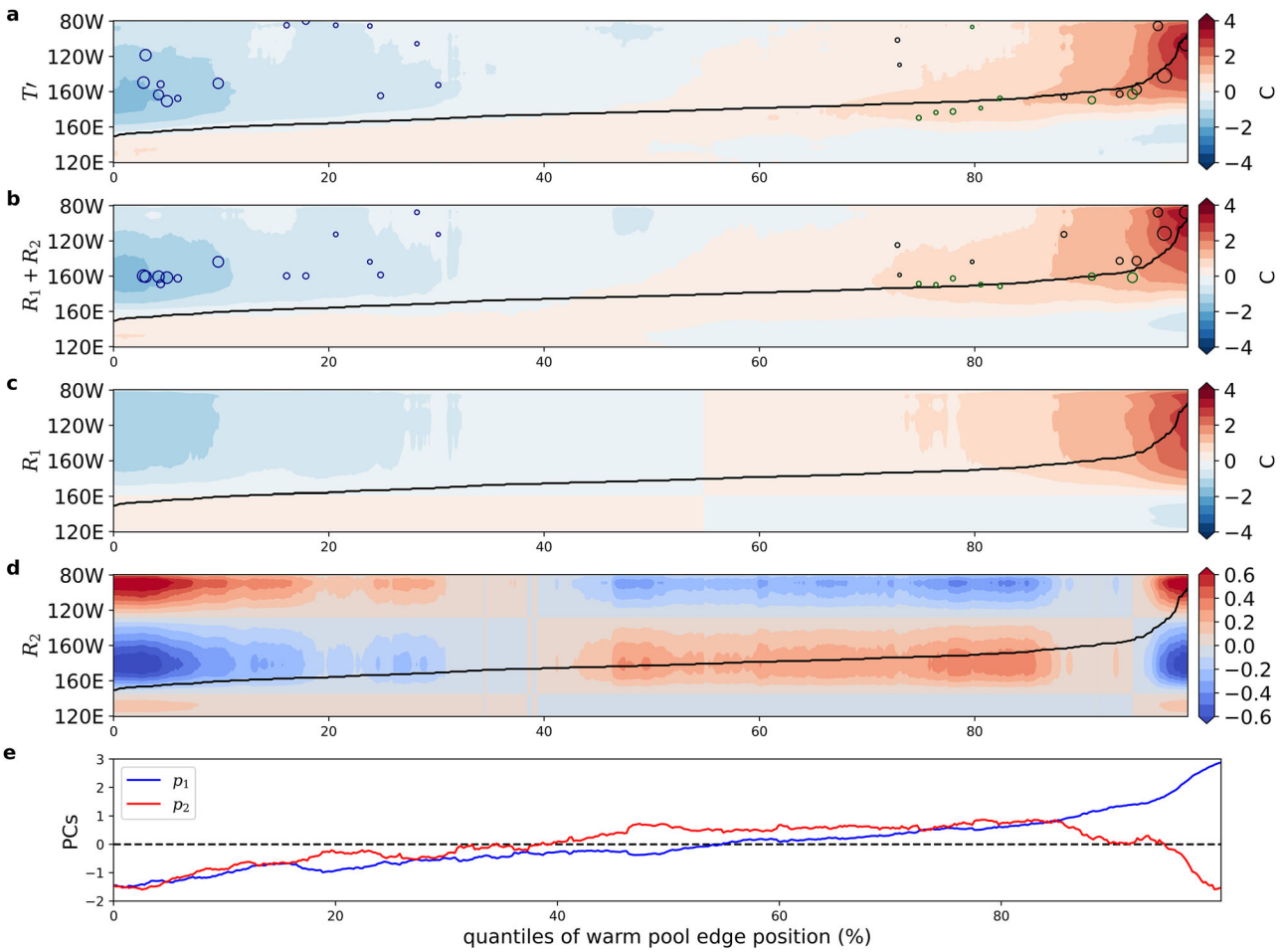

Fig. 15 | Pattern continuum of T and its PCA. Same as Fig. 4 but for observed SST T, and here smoothed. **a** Pattern continuum of SSTA flow T', quantile-ordered with WPEP. WPEP is indicated (black line). **b** Same as **a** for R_1+R_2 as deduced from PCA of T'. In (**a**, **b**) we overplot the location of individual ENSO event peaks as in Fig. 1e. **c** Same as **a** for $R_1=E_1p_1$. **d** Same as a for $R_2=R_2p_2$. **e** Principal components p_1, p_2 ordered into quantiles for WPEP.

SST flows intercomparison

In the present paper, we have examined various SST flows, which for clarity are summarized in Table 1. These flows are approximations of the "true" observed SST flow T, with the same shape but potentially lower dimensionality (i.e., degrees of freedom), as obtained from various means (e.g., projection, filtering, or averaging, etc). T_{qs} is the flow resulting from the pattern continuum smoothing of T. $\widetilde{T}$ is the shifted-mean flow ($\widetilde{T}_{ideal}$ is another shifted-mean flow not listed for brevity). T'_{12} is the PCA truncation of T', while $\widetilde{T}'_{12}$ is the PCA truncation of $\widetilde{T}'$ ($\widetilde{T}_{12}$ is considered mainly to demonstrate the mechanisms of PCA decomposition).

Figure 12 compares reconstruction errors, that is, flow differences with T (or T'). Reconstruction errors of the shifted mean flow $\widetilde{T}$ and quantile-smoothed flow T_{qs} are rather similar (and they arise when WPEP is unrepresentative of the actual SSTA pattern). These flows miss various moderate warmings/coolings in the EP as well as intense warming in the aftermath of 1982 and 1998 super El Niños. In the aftermath of 1982 and 1998, warm SSTs lingered unusually long in the far EP while the WPEP shifted back westward. These rather unique scenarios were likely due to strong meridional wind shifting preventing seasonal surface cooling, a nonlinear mechanism separate from the present zonal spatial shifting[29–32]. Note also that WPEP estimation is unclear over these periods, as the non-seasonal and

seasonal estimates are markedly different (Fig. 6b). The PCA-truncated flow T'_{12} performs better as it fits data with an additional degree of freedom and no smoothing. Its score is potentially improved by capturing non-ENSO fluctuations in T', which is hard to disentangle.

In Figs. 13 and 14, we plot SST and SSTA profiles for all ENSO events (1980–2022) at their peak. We compare this between observations T and the shifted-mean flow $\widetilde{T}$ (Figs. 13 and 14). There is a good agreement overall. The most important discrepancies are for extreme El Niños 1997, 2015, 1982 (each is spatially very unique, thus our composite approach is necessarily limited), La Niñas 1996, 1999, 2007, 1988 (central-EP cooling is underestimated), as well as 2016, 2017 (strictly in the far-east).

Finally, Fig. 15 shows the pattern continuums of T' and its PCA truncation T'_{12}. The intuition is similar to Fig. 4 (for $\widetilde{T}'$ and $\widetilde{T}'_{12}$), that is R_1 and R_2 combine nonlinearly to grasp SST patterns with a roughly linear(-quadratic) dependency of p_1 (p_2) on χ. Recall, however, that $\widetilde{T}'$ is univariate, thus its PCA decomposition is comparatively more tractable.

Data availability

The datasets analyzed during the current study are available at the following repositories. https://www.psl.noaa.gov/data/gridded/data.godas.htmlhttps://www.cesm.ucar.edu/community-projects/lenshttps://psl.noaa.gov/data/gridded/data.noaa.ersst.v5.htmlhttps://climatedataguide.ucar.edu/climate-data/sst-data-hadisst-v11.

Received: 24 April 2025; Accepted: 12 September 2025;
Published online: 05 November 2025

References

1. Ropelewski, C. F. & Halpert, M. S. Global and regional scale precipitation patterns associated with the El Niño southern oscillation. *Mon. Weather Rev.* **115**, 1606–1626 (1987).
2. McPhaden, M. J., Zebiak, S. E. & Glantz, M. H. ENSO as an integrating concept in earth science. *Science* **314**, 1740–1745 (2006).
3. L'Heureux, M. L. et al. Enso prediction. *El Niño Southern Oscillation in a Changing Climate* 227–246 (AGU, 2020).
4. Timmermann, A. et al. El Niño–Southern oscillation complexity. *Nature* **559**, 535–545 (2018).
5. Capotondi, A., Wittenberg, A., Kug, J.-S., Takahashi, K. & PcPhaden, M. Enso diversity. In *El Niño Southern Oscillation in a Changing Climate* (eds. McPhaden, M., Santoso, A. & Cai, W.) Vol. 253, 65–86 (AGU, Washington DC, 2020).
6. Kug, J.-S., Jin, F.-F. & An, S.-I. Two types of El Niño events: cold tongue El Niño and warm pool El Niño. *J. Clim.* **22**, 1499–1515 (2009).
7. Rasmusson, E. M. & Carpenter, T. H. Variations in tropical sea surface temperature and surface wind fields associated with the southern oscillation/El Niño. *Mon. Weather Rev.* **110**, 354–384 (1982).
8. An, S.-I., Tziperman, E., Okumura, Y. M. & Li, T. Enso irregularity and asymmetry. In *El Niño Southern Oscillation in a Changing Climate*, vol. 253, 153–172 (AGU, Washington DC, 2020).
9. Bjerknes, J. Atmospheric teleconnections from the equatorial Pacific. *Mon. Weather Rev.* **97**, 163–172 (1969).
10. Thual, S. & Dewitte, B. Enso complexity controlled by zonal shifts in the walker circulation. *Nat. Geosci.* **16**, 328–332 (2023).
11. McPhaden, M. & Picaut, J. El niño-southern oscillation displacements of the western equatorial pacific warm pool. *Science* **250**, 1385–1388 (1990).
12. Yan, Z., Wu, B., Li, T. & Tan, G. Mechanisms determining diversity of enso-driven equatorial precipitation anomalies. *J. Clim.* **35**, 923–939 (2022).
13. Picaut, J., Masia, F. & du Penhoat, Y. An advective-reflective conceptual model for the oscillatory nature of the ENSO. *Science* **277**, 663–666 (1997).
14. Clarke, A. J., Wang, J. & Van Gorder, S. A simple warm-pool displacement ENSO model. *J. Phys. Oceanogr.* **30**, 1679–1691 (2000).
15. Schopf, P. S. & Burgman, R. J. A simple mechanism for ENSO residuals and asymmetry. *J. Clim.* **19**, 3167–3179 (2006).
16. Jin, F.-F. An equatorial ocean recharge paradigm for ENSO. Part I: conceptual model. *J. Atmos. Sci.* **54**, 811–829 (1997).
17. Jin, F.-F. et al. Simple ENSO models. In (eds. McPhaden, M., Santoso, A. & Cai, W.) *El Niño Southern Oscillation in a Changing Climate*, Vol. 253, 119–151 (AGU, Washington DC, 2020).
18. Picaut, J., Ioualalen, M., Menkès, C., Delcroix, T. & Mcphaden, M. J. Mechanism of the zonal displacements of the Pacific warm pool: Implications for ENSO. *Science* **274**, 1486–1489 (1996).
19. Picaut, J. et al. The oceanic zone of convergence on the eastern edge of the Pacific warm pool: a synthesis of results and implications for El Niño-Southern Oscillation and biogeochemical phenomena. *J. Geophys. Res. Oceans* **106**, 2363–2386 (2001).
20. Brown, J. N., Langlais, C. & Gupta, A. S. Projected sea surface temperature changes in the equatorial Pacific relative to the warm pool edge. *Deep Sea Res. Part II Topical Stud. Oceanogr.* **113**, 47–58 (2015).
21. Capotondi, A. et al. Understanding ENSO diversity. *Bull. Am. Meteorol. Soc.* **96**, 921–938 (2015).
22. Williams, I. N. & Patricola, C. M. Diversity of ENSO events unified by convective threshold sea surface temperature: a nonlinear ENSO index. *Geophys. Res. Lett.* **45**, 9236–9244 (2018).
23. Behringer, D. & Xue, Y. Evaluation of the global ocean data assimilation system at NCEP: the Pacific Ocean. In *Eighth Symp. on Integrated Observing and Assimilation Systems for Atmosphere, Oceans, and Land Surface* xx–yy (NCEP, 2004).
24. Dommenget, D., Bayr, T. & Frauen, C. Analysis of the non-linearity in the pattern and time evolution of El Niño Southern Oscillation. *Clim. Dyn.* **40**, 2825–2847 (2013).
25. Kug, J.-S. & Ham, Y.-G. Are there two types of La Niña? *Geophys. Res. Lett.* https://doi.org/10.1029/2011GL048237 (2011).
26. Takahashi, K., Montecinos, A., Goubanova, K. & Dewitte, B. ENSO regimes: reinterpreting the canonical and Modoki El Niño. *Geophys. Res. Lett*. https://doi.org/10.1029/2011GL047364 (2011).
27. Fedorov, A. V., Brown, J. N. & Steele, J. *Equatorial Waves* (Academic Press, 2009).
28. Takahashi, K. & Martínez, A. G. The very strong coastal El Niño in 1925 in the far-eastern Pacific. *Clim. Dyn.* **52**, 7389–7415 (2019).
29. Vecchi, G. A. & Harrison, D. The termination of the 1997–98 El Niño. Part I: mechanisms of oceanic change. *J. Clim.* **19**, 2633–2646 (2006).
30. Vecchi, G. A. The termination of the 1997–98 El Niño. Part II: mechanisms of atmospheric change. *J. Clim.* **19**, 2647–2664 (2006).
31. Stuecker, M. F., Timmermann, A., Jin, F.-F., McGregor, S. & Ren, H.-L. A combination mode of the annual cycle and the El Niño Southern Oscillation. *Nat. Geosci.* **6**, 540–544 (2013).
32. McGregor, S. et al. Meridional movement of wind anomalies during enso events and their role in event termination. *Geophys. Res. Lett.* **40**, 749–754 (2013).
33. Burgers, G. & Stephenson, D. B. The "normality" of El Niño. *Geophys. Res. Lett.* **26**, 1027–1030 (1999).
34. Boucharel, J. et al. Enso nonlinearity in a warming climate. *Clim. Dyn.* **37**, 2045–2065 (2011).
35. Frauen, C. & Dommenget, D. El niño and La Niña amplitude asymmetry caused by atmospheric feedbacks. *Geophys. Res. Lett*. https://doi.org/10.1029/2010GL044444 (2010).
36. Thual, S., Majda, A. J., Chen, N. & Stechmann, S. N. Simple stochastic model for El Niño with westerly wind bursts. *Proc. Natl. Acad. Sci. USA* **113**, 10245–10250 (2016).
37. Chen, N., Fang, X. & Yu, J.-Y. A multiscale model for El Niño complexity. *npj Clim. Atmos. Sci*. **5**, 16 (2022).
38. Karamperidou, C., Jin, F.-F. & Conroy, J. L. The importance of ENSO nonlinearities in tropical Pacific response to external forcing. *Clim. Dyn.* **49**, 2695–2704 (2017).
39. Cai, W. et al. Increased variability of eastern Pacific el Niño under greenhouse warming. *Nature* **564**, 201–206 (2018).

40. Schlör, J., Strnad, F., Capotondi, A. & Goswami, B. Contribution of El Niño Southern Oscillation (ENSO) diversity to low-frequency changes in ENSO variance. *Geophys. Res. Lett.* **51**, e2024GL109179 (2024).
41. Björnsson, H. & Venegas, S. A manual for EOF and SVD analyses of climatic data. *CCGCR Rep.* **97**, 112–134 (1997).
42. Takahashi, K., Karamperidou, C. & Dewitte, B. A theoretical model of strong and moderate El Niño regimes. *Clim. Dyn.* **52**, 7477–7493 (2019).
43. Geng, T., Cai, W. & Wu, L. Two types of ENSO varying in tandem facilitated by nonlinear atmospheric convection. *Geophys. Res. Lett.* **47**, e2020GL088784 (2020).
44. Hu, S. & Fedorov, A. V. Cross-equatorial winds control El Niño diversity and change. *Nat. Clim. Change* **8**, 798–802 (2018).
45. Guilyardi, E., Capotondi, A., Lengaigne, M., Thual, S. & Wittenberg, A. T. ENSO modeling: History, Progress and Challenges. In McPhaden, M., Santoso, A. & Cai, W. (eds.) *El Niño Southern Oscillation in a Changing Climate*, 253, 199–226 (AGU, Washington DC, 2020).
46. Neelin, J. D. et al. ENSO theory. *J. Geophys. Res.* **103**, 14261–14290 (1998).
47. Cai, W. et al. Pantropical climate interactions. *Science* **363**, eaav4236 (2019).
48. Bayr, T., Dommenget, D., Martin, T. & Power, S. B. The eastward shift of the Walker circulation in response to global warming and its relationship to ENSO variability. *Clim. Dyn.* **43**, 2747–2763 (2014).
49. Fedorov, A. V., Hu, S., Wittenberg, A. T., Levine, A. F. Z. & Deser, C. ENSO low-frequency modulation and mean state interactions. In (eds. McPhaden, M., Santoso, A. & Cai, W.) *El Niño Southern Oscillation in a Changing Climate*, Vol. 253, 173–198 (AGU, Washington DC, 2020).
50. Kay, J. E. et al. The community earth system model (cesm) large ensemble project: a community resource for studying climate change in the presence of internal climate variability. *Bull. Am. Meteorol. Soc.* **96**, 1333–1349 (2015).
51. Deser, C. et al. Enso and Pacific decadal variability in the Community Climate System Model version 4. *J. Clim.* **25**, 2622–2651 (2012).
52. Capotondi, A., Deser, C., Phillips, A., Okumura, Y. & Larson, S. Enso and Pacific decadal variability in the Community Earth System Model version 2. *J. Adv. Model. Earth Syst.* **12**, e2019MS002022 (2020).
53. Huang, B. et al. Extended reconstructed sea surface temperature, version 5 (ersstv5): upgrades, validations, and intercomparisons. *J. Clim.* **30**, 8179–8205 (2017).
54. Rayner, N. A. et al. Global analyses of sea surface temperature, sea ice, and night marine air temperature since the late nineteenth century. *J. Geophys. Res. Atmos.* **108**, 4407 (2003).

Acknowledgements

The research of S.T. was supported by ANR (grant ANR-18-CE01-0012). B.D. acknowledges support from ANID (Concurso de Fortalecimiento al Desarrollo Científico de Centros Regionales 2020-R20F0008-CEAZA, COPAS COASTAL FB210021 and Fondecyt Regular 1231174) and ANR (Grant ANR-18-CE01-0012). The authors also acknowledge support from ANR Templex (grant ANR-23-CE56-0002).

Author contributions

S.T. designed and performed research. S.T. and B.D. discussed research and wrote the paper.

Competing interests

The authors declare no competing interests.

Additional information

Correspondence and requests for materials should be addressed to Sulian Thual.